



**HAL**  
open science

## Effect of end milling, grinding and tartaric-sulfuric anodizing on the fatigue behavior of AA7050 alloy

Foued Abroug, Etienne Pessard, Guénaël Germain, Franck Morel

► **To cite this version:**

Foued Abroug, Etienne Pessard, Guénaël Germain, Franck Morel. Effect of end milling, grinding and tartaric-sulfuric anodizing on the fatigue behavior of AA7050 alloy. *International Journal of Advanced Manufacturing Technology*, 2022, 122 (9-10), pp.3903-3922. 10.1007/s00170-022-10124-3 . hal-03801227

**HAL Id: hal-03801227**

**<https://hal.science/hal-03801227>**

Submitted on 6 Oct 2022

**HAL** is a multi-disciplinary open access archive for the deposit and dissemination of scientific research documents, whether they are published or not. The documents may come from teaching and research institutions in France or abroad, or from public or private research centers.

L'archive ouverte pluridisciplinaire **HAL**, est destinée au dépôt et à la diffusion de documents scientifiques de niveau recherche, publiés ou non, émanant des établissements d'enseignement et de recherche français ou étrangers, des laboratoires publics ou privés.

# Effect of end milling, grinding and tartaric-sulfuric anodizing on the fatigue behavior of AA7050 alloy

Foued Abroug<sup>1,2</sup> · Etienne Pessard<sup>1</sup> · Guenaël Germain<sup>1</sup> · Franck Morel<sup>1</sup>

## Abstract

The present study investigates the effect of the high-speed milling (HSM), grinding and anodizing processes on the high cycle fatigue strength of the AA7050 aluminum alloy. These processes are systematically applied to certain aircraft components as specified by aeronautical standards, to attain a good surface finish. In order to understand the effect of each process on the fatigue strength, a vast experimental campaign consisting of fully reversed plane bending fatigue tests has been conducted on specimens with different surface states. A polished batch, three milled batches with different surface roughness, a grinded batch and two milled then anodized batches with different surface roughness have been tested. The results show that the roughness must be highly degraded ( $Sa > 3 \mu m$ ) in order to impact the fatigue strength. It is also shown that anodizing has slight beneficial effect on the fatigue strength in the high cycle fatigue domain studied. The experimental results show a dependence of the fatigue strength on the surface roughness via the parameter  $\sqrt{Sa}$ , previously proposed by the authors.

**Keywords** High-speed milling · Grinding · TSA anodizing · Surface roughness · High cycle fatigue

## 1 Introduction

In the aerospace industry, a large number of parts are manufactured via end milling. This process induces thermomechanical effects that can impact the surface integrity of the part (surface roughness, residual stresses as well as work hardening) and therefore its in-service life [1–3]. In addition, surface defects caused by milling can be created, accidentally or otherwise. These defects can cause stress concentrations, which during service could lead to fracture. Hence, the aircraft industry needs to define acceptability surface criteria for milled parts prior to their usage.

The impact of the milling process on the fatigue behavior of aircraft components has been the subject of several studies. One of the main results of these studies is that surface roughness is the major factor controlling the fatigue behavior of end milled AA7XXX parts [2]. Residual stresses and microstructural changes have been found however to have

a secondary role in terms of fatigue [3, 4]. Note that this is not always the case, especially in rolling milling for which the residual stresses could have an important effect on the fatigue behavior [2].

Two main finishing processes are often applied to aircraft components. Firstly, manual local grinding is done to erase eventual surface defects or undesired surface roughness. Although the term is the same, a lot of studies address grinding using a grinding wheel [5–8], whereas grinding using abrasive paper or a flap wheel is rarely addressed in the literature, in particular from a fatigue strength point of view [9, 10]. Nonetheless, these studies showed that grinding results in a lower fatigue strength than that generated by machining. Fatigue cracks for grinded parts were found via FE analysis to initiate at the bottom of the grooves that generate the highest stress concentration value [10].

Secondly, a surface treatment for aluminum alloy components is applied with the aim of enhancing the corrosion resistance. During the surface treatment, components firstly undergo a pickling operation to erase the potential residual stress gradient and hardening induced by milling at the upper surface, as well as to chemically clean it. Then an anodizing process is applied to cover the surface by a thin protective oxide layer. The pickling operation removes less than 10 micrometers from the surface and results in a modification

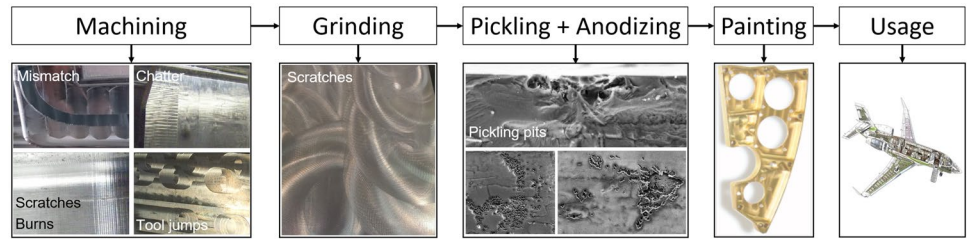
---

✉ Foued Abroug  
Foued.Abroug@enit.fr

<sup>1</sup> LAMPA, Arts et Métiers ParisTech Angers, 2 Bd du Ronceray, 49035 Angers, France

<sup>2</sup> LGP, ENIT - Tarbes, 47 Avenue d'Azereix, 65000 Tarbes, France

**Fig. 1** Steps of aircraft aluminum components manufacturing



of its topography and could introduce pits during the pickling process [11, 12]. The anodization does not systematically succeed in filling these pits with the alumina layer. According to the literature [4, 11, 13], the surface treatment often reduces the fatigue strength of the component, this is the case for studies using chromic and sulfuric anodizing treatments. Some studies, on the other hand, show that tartaric-sulfuric anodizing (TSA) preserves the high cycle fatigue strength of the parts [13, 14], but studies on the HCF of the TSA process remain rare in the literature [15]. The chronology of the operations that AA7050 aircraft components undergo is presented in Fig. 1.

The authors have presented in a previous study the effect of surface roughness, induced by end milling, on the fatigue behavior of AA7050 parts [16]. This paper showed that both stress concentration and the size of the highly stressed volume induced by the surface topography control the fatigue life of the components.

The aim of the present work is to study the effect of grinding and the TSA process on the fatigue behavior of aircraft

components. Three additional specimen batches are presented in the present paper and tested in fatigue. These batches are obtained either by manual grinding or by tartaric-sulfuric anodizing, both complementary operations to the milling process. The results are compared to previous results and allow the impact on fatigue of these particular manufacturing operations to be quantified. In addition to fatigue strength, the damage mechanism of each batch is identified and discussed. A link between surface roughness and the fatigue strength will also be established.

## 2 The investigated material and the experimental setup

### 2.1 The material

The investigated material is a 30 mm thick rolled sheet of AA 7050 Aluminum alloy (Al Zn6CuMgZr) intended for aeronautical applications. The chemical composition of the AA7050-T7451 alloy (in Wt%) is: 6.027 Zn, 2.221 Cu, 1.847 Mg, 0.102 Zr, 0.039 Ti, 0.038 Si, 0.095 Fe, 0.01 Mn. The microstructure of the sheet used is shown in Fig. 2. The rolling

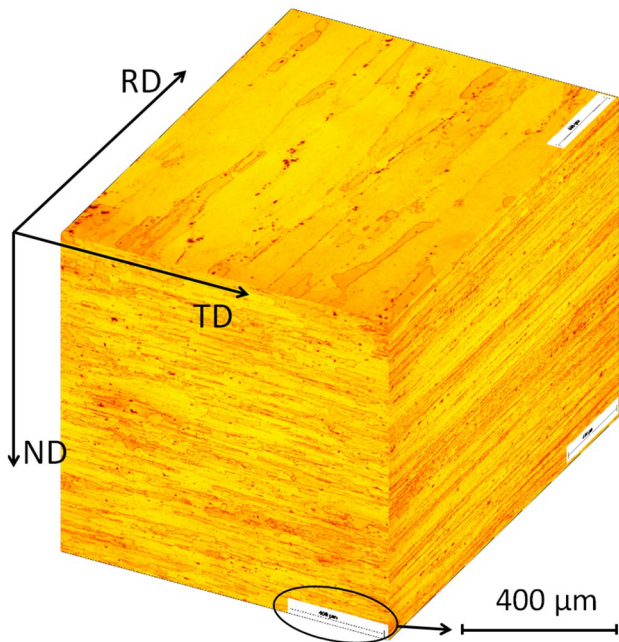


**Fig. 2** Microstructure of the AA7050-T7451 alloy (RD = Rolling Direction 0°, TD = Transverse Direction 90°, ND = Normal Direction)

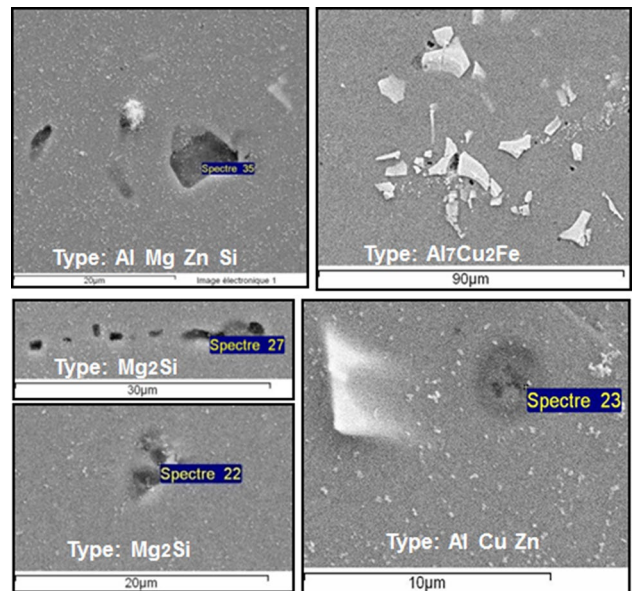
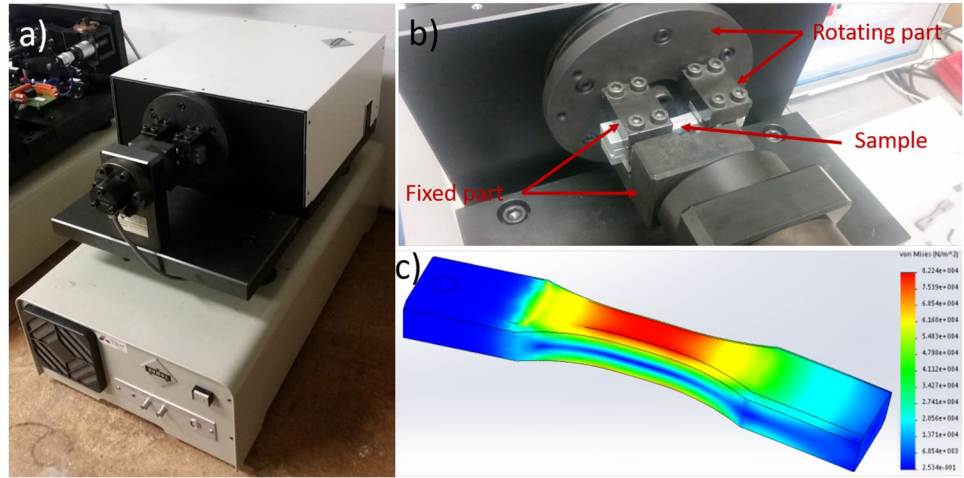


**Fig. 3** Al<sub>7</sub>Cu<sub>2</sub>Fe, Al Mg Zn Si and Mg<sub>2</sub>Si type intermetallic particles at the surface of the AA7050 alloy

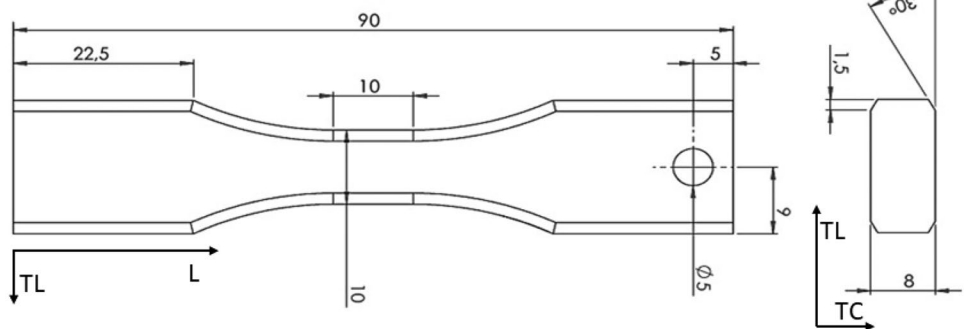
**Fig. 4** a) Rumul Cracktronic fatigue test machine, b) a zoomed view on the loading zone and c) stress distribution resulting from plane bending



process generated a high degree of recrystallization. The areas of consolidation of recrystallized and non-recrystallized grains can be up to a few millimeters in length. The range of grain sizes is between 5 and 300  $\mu\text{m}$  in the rolling and the transverse directions, and between 5 and 50  $\mu\text{m}$  in the depth direction (see Fig. 2). Intermetallic particles, mainly located at the grain boundaries and in the recrystallized grains, are also present. For the AA7050 alloy, the majority of these particles, whose size can be up to 20  $\mu\text{m}$  in length, are of type  $\text{Mg}_2\text{Si}$  and  $\text{Al}_7\text{Cu}_2\text{Fe}$ . Particles of  $\text{MgZn}_2$  and  $\text{AlCuZn}$  are also present in the structure (see Fig. 3). These brittle particles are known to be at the origin of the initiation of fatigue cracks in aluminum alloys [17, 18].

Monotonic tensile tests have been conducted in accordance with the ASTM E8M-04 and NF EN 2002-001 04-2006 standards to determine the mechanical properties of the AA7050-T7451 alloy. The results are; Yield Stress of 475, 428 and 475 MPa; Ultimate Tensile Stress of 635, 496 and 538 MPa; and Tensile elongation of 12.3%, 13.9% and 11.9% in the 0°, 45° and 90° direction relative to the rolling direction, respectively. The material is anisotropic, its behavior appears to be similar in the 0° and 90° directions, whereas the 45° direction has higher ductility with an elongation of 13.9%. Microhardness measurements conducted in the Normal Direction show slight variations around 157 Hv/0.5.

**Fig. 5** Geometry of plane bending sample



## 2.2 Experimental work

Fatigue tests have been carried out on a Rumul Cracktronic, resonant fatigue testing machine (see Fig. 4) under the following conditions:

- Fully reversed plane bending load ( $R = -1$ ).
- Test frequency :  $\approx 75$  Hz.
- Ambient temperature and pressure, ambient air.
- Stopping criterion: frequency drop of 0.70 Hz corresponding to the presence of a crack on the specimen (crack larger than 5 mm), or  $2 \times 10^6$  cycles reached.

The fatigue tests were carried out using the Staircase method described by Dixon and Mood [19] and the ISO12107 standard [20]. The fatigue strength was assessed at  $2 \times 10^6$  cycles and a step of 10 MPa was used for the staircase. For the different batches, 10 to 15 samples are tested per batch. Specimens that survived the staircase procedure were retested at a higher load, in order to obtain an overview of the SN curve shape in the finite fatigue life regime.

The nature of the fully reversed plane bending loads, which implies the presence of a bending gradient, makes this loading mode ideal to characterize the effect of the specimen surfaces on the fatigue behavior (see Fig. 4). The geometry

**Table 1** milling conditions for the AA7050 alloy

Surface state	Spindle (rpm)	Feed per tooth (mm/tooth/rd)	Number of teeth	Tool's nose radius (mm)	Tool's Diameter (mm)	Tilt tool/piece
M1.1	24 000	0.15	2	4	Ø10	0°
M4.2	10 000	0.55	2	0.8	Ø20	0.014°
M5.5	10 000	0.55	2	0.8	Ø20	0.05°

of the specimen is shown in Fig. 5. All specimens are taken from the middle of the sheet with the loading axis parallel to the rolling direction. A 30° chamfer is machined on the specimen edges to avoid crack initiation at the edges.

To identify the effect of the various manufacturing processes on fatigue, different batches of specimens were prepared. A first batch of polished specimens, referred to as batch P0, is used as a reference to characterize the nominal fatigue limit at  $2 \times 10^6$  cycles of the material without surface defects. Polishing was done using silicon carbide papers of 1200 and 2400 particle size, with water lubrication. After polishing, 3D surface scans of the specimens were made using a Bruker Contour GT-K0-X optical profilometer and the surface roughness  $Sa$  is found to be of  $0.04 \mu\text{m}$ .

The impact of the surface state introduced by high-speed milling (HSM) is subsequently studied. Three milled surface states were prepared. The first is representative of the standard machined surface state achieved under optimal end milling conditions. This batch is noted M1.1. The other surface states are prepared using highly degraded milling conditions and are denoted M4.2 and M5.5. The milling conditions for the 3 batches have been discussed in reference [16] and are summarized in Table 1.

In addition, a grinded batch was prepared by industrial means, in the same conditions as the industrial components. This batch, noted G3.8 (Fig. 6a), represents the

industrial surface condition obtained after grinding of a milled surface defect. The specimens were manually grinded using first a vibrating grinder with 40 grit sandpaper, followed by a second step with a straight grinder with 80 grit sandpaper (average grain size of the order of  $400 \mu\text{m}$  and  $200 \mu\text{m}$  respectively) (see Fig. 6). The abrasive paper was changed at the beginning of grinding.

Finally, two batches made by end milling in the same conditions as the M1.1 and the M5.5 batches were prepared. These two batches then underwent an anodizing treatment. In order to respect the requirements of the REACH2017 program to eliminate the use of hexavalent chromium for toxicity reasons, the authors focused on the tartaric-sulfuric substitution treatment (TSA) and its contribution to the fatigue behavior of the AA7050 substrate. The TSA surface treatment was carried out according to the standardized industrial process and was composed of a Turco-Smutgo pickling and a tartaric-sulfuric anodizing operation. The complete sequence is presented in Table 2. The anodized batches are named M0.9-TSA and M5.4-TSA. Table 3 summarizes all the surface states prepared for fatigue testing.

### 2.3 Surface states characterization

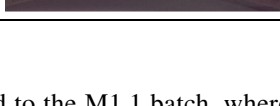
The different surface states were scanned and analyzed using the Bruker Contour GT-K0-X optical profilometer. The surface topologies are shown in Figs. 7 and 8. A large difference is observed between the M1.1, M4.2 and the M5.5 surface states. The high feed rate values for the M4.2 and M5.5 batches generate a tool path leaving areas of high altitude and generates high roughness, both on the total surface (parameter  $Sa$  shown in Table 4) and over high peak lines (parameter  $Ra_{max}$  shown in Table 4 and profiles shown in Fig. 11). Figure 7 also shows the grinded surface scan where the profile is mostly chaotic with scratches crossing the width of the specimen. However, the all-over surface roughness does not seem as affected as by the presence of high peaks on the M4.2 and the M5.5 surface states. As for

**Fig. 6** Grinding steps by industrial means, **a** vibrating grinder and **b** straight grinder with a grit 40 and grit 80 sandpaper respectively**Table 2** TSA surface treatment sequence of the AA7050-T7451 alloy

Soda pickling	Degreasing Turco + rinsing + Soda (NaOH) pickling for $3 \text{ min } 45 \pm 10 \text{ sec}$
Pickling	Pickling Smutgo + rinsing + Pickling Smutgo
Anodization	tartaric-sulfuric solution of $C_4H_6O_6/H_2SO_4$

**Table 3** Summary of the different surface state batches for fatigue testing

TABLE 3: Summary of the different surface state batches for fatigue testing.

Surface State	Batch Notation	$\bar{S}a$ ( $\mu m$ )	Process	Samples /batch	Topography
Polished	P0	0.04	Manual polishing	15	
milled (Standard)	M1.1	1.1	End milling	15	
milled (degraded-1)	M4.2	4.2	End milling	15	
milled (degraded-2)	M5.5	5.5	End milling	10	
Grinded	G3.8	3.8	Manual grinding	10	
Anodized	M0.9-TSA	0.9	Milling + etching	15	
	M5.4-TSA	5.4	+ anodizing	10	

the chemical process, Fig. 8 shows an example of a specimen from the M5.4-TSA batch post-anodizing surface treatment. The 3D scans show that the surface topology is only slightly affected on a macroscopic scale. However, on a more local scale, pits can be observed at the surface and at the bottom of the milling grooves.

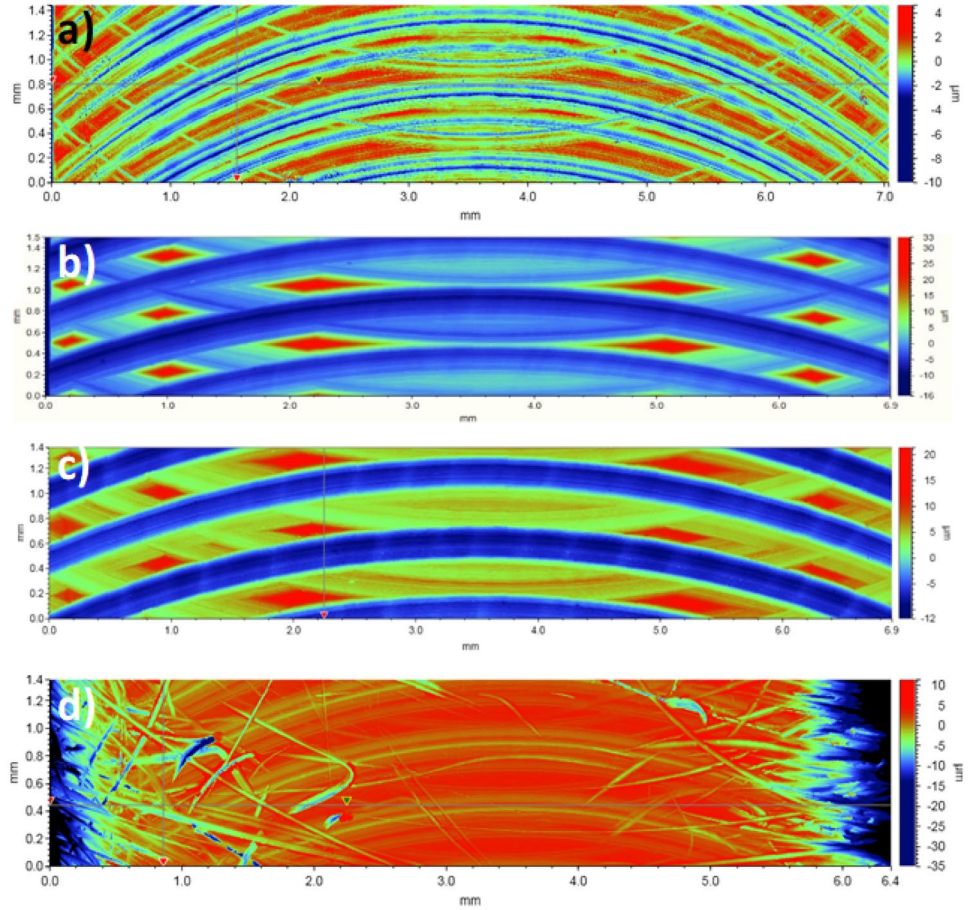
For the anodized specimens, optical microscope and SEM observations were made after each step of the surface treatment process. The anodic layer has a thickness of between 2 and 3  $\mu m$  (Fig. 10c). After pickling, pits are created and are located at the grain boundaries and within the recrystallized grains (Fig. 10a). These pits can reach widths of the order of 15  $\mu m$  and depths of the order of 15  $\mu m$  (Fig. 10c). Networks of small pits can be observed and are of length of the order of 300  $\mu m$  (Fig. 10a). After anodizing, the anodic layer completely covers the pickling pits. No decohesion zone between the substrate and the anodized layer was detected. The TSA does not seem to affect the size of the pits created during the pickling process (see Fig. 9). Figure 9 shows that the milling grooves are still visible on the surface after the pickling and anodizing processes.

2D roughness profiles were also collected for each surface state and are shown in Figs. 11 and 12. Figure 11 shows the surface profiles for the milled and grinded configurations. The milling grooves are wider and deeper for the M4.2 and

M5.5 batches when compared to the M1.1 batch, whereas the grinding scratches appear to be sharper and less regular (Fig. 11). Figure 12 shows an example of surface profiles before and after surface TSA treatment (profile for the M5.5 and the M5.4-TSA batches). The general aspect remained mostly the same, however, for the M5.4-TSA batch, the profile has a rougher appearance after the chemical treatment. As shown in Fig. 9, the anodizing process did not change the surface appearance obtained after pickling. Hence, it is assumed that the rough aspect shown in Fig. 12 is due mainly to the pickling process. The role of anodizing is to add a thin protective layer of approximately constant thickness of around 3  $\mu m$  as shown in Fig. 10c.

The surface topography for the different surface states is assessed via the  $Sa$  and  $Ra_{max}$  roughness parameters as shown in Table 4.  $Sa$  offers an average roughness value for the entire surface of the specimen and expressed via Eq. 1, whereas  $Ra_{max}$  represents the maximum arithmetic roughness value measured over the width of the gauge length of a specimen and is expressed via Eq. 2. When comparing the  $Sa$  versus the  $Ra_{max}$  values for the surface states of the M4.2, M5.5 and M5.4-TSA batches, it is observed that the M4.2 has a lower  $Sa$  value than that of the M5.5 and M5.4-TSA batches. However, its value of  $Ra_{max}$  is higher. As for the anodized specimens, despite the presence of pits on the surface of the specimens

**Fig. 7** Surface topography of milled and grinded specimens



(see Fig. 9), the surface roughness  $Sa$  before and after surface treatment remain very similar.  $Sa$  values go from  $1.1 \mu\text{m}$  to  $0.9 \mu\text{m}$  for the M0.9-TSA batch and from  $5.5 \mu\text{m}$  to  $5.4 \mu\text{m}$  for the M5.4-TSA batch.

$$Sa = \frac{1}{S} \iint_S |Z(x, y)| dx dy \quad (1)$$

$$Ra = \frac{1}{l_n} \int_0^{l_n} |Z(x)| dx \quad (2)$$

### 3 Experimental results

#### 3.1 Fatigue test results

This section presents the fatigue test results for the different batches presented in the previous section. The data is presented in the form of S-N curves. The results of the Staircase fatigue tests are summarized in Table 5. In addition, in order to understand the mechanisms that control the fatigue damage of each surface state and roughness, SEM fractographic observations and crack localization analyses are conducted.

##### 3.1.1 Fatigue strength of the polished reference state

For the polished reference state P0, the estimated fatigue limit at  $2 \times 10^6$  is 174 MPa with low scatter (see Table 5). The associated standard deviation is estimated according to Dixon and Mood [19] at 5.3 MPa (0.53 X step of the StairCase).

As shown in Fig. 13, for 66% of the tested specimens crack initiation is clearly located at the intermetallic particles. EDX analysis of these particles shows that they are either  $Mg_2Si$  or  $Al_7Cu_2Fe$  particles. For the rest of the cases, cracks initiate from areas without visible particle, but rich with Mg and Zn as identified via EDX analyses (Fig. 13b). According to [21], the high concentration of these elements may indicate the presence of nanometric precipitates of  $MgZn_2$ , which may be at the origin of the crack initiation. The two mechanisms (particles or areas rich in additive elements) coexist at low and high loading levels.

##### 3.1.2 Effect of milling on the fatigue behavior

After machining, the fatigue strength obtained for the M1.1 state is equal to 159 MPa and therefore has a reduction of 15

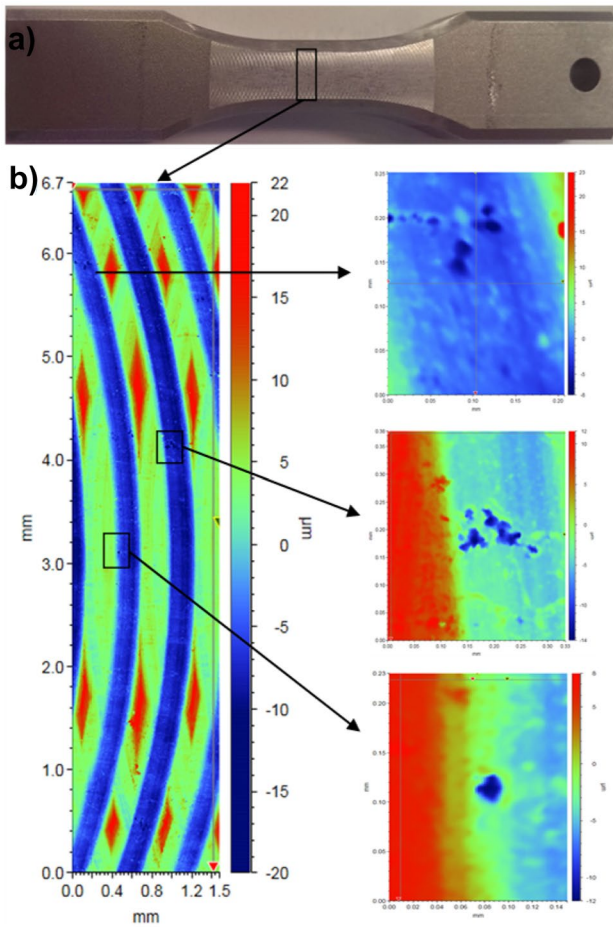


**Fig. 8** M5.4-TSA **a** specimen and **b** 3D surface scan with a zoom over local pits

MPa compared to the P0 reference state. The average fatigue limit of the M4.2 state shows a greater decrease and reaches 141 MPa. The fatigue decrease is the most pronounced for the M5.5 Batch (-55 MPa) compared to the reference state P0. The associated standard deviation for all milled surface states remains low, of the order of 5.3 MPa (see Table 5). The S-N curves of the polished and milled batches are shown in Fig. 14.

The slope of the S-N curves for the polished and milled batches are similar. In addition, observation of the S-N curves for the different batches shows that the fatigue strength seems constant over a large number of cycles, which suggests the existence of a fatigue limit asymptote. To verify this hypothesis, a specimen of the M1.1 batch was loaded at 150 MPa (a loading step below the fatigue limit determined by the StairCase method) for a very large number of cycles. For this specimen, the test was stopped at  $2.2 \cdot 10^7$  cycles and no cracks were observed. This test validates the concept of

an endurance limit reached at  $10^6$  cycles for the AA7050 aluminum alloy tested in bending.

As for the damage mechanisms, the principally observed crack initiation mechanism for the M1.1 surface state is the initiation at the intermetallic particles. This is observed at high and low cycles domains. At high stress amplitude loading level, multiple crack initiation sites are observed. This result agrees with the observations made by [22] on an AA7050 alloy. Only one of the 15 tested specimens did not have a particle at the initiation site at a high cycle level (Fig. 15b).

In the case of the M4.2 surface state, two damage mechanisms are present depending on the loading level. Intermetallic particles are present at the crack initiation sites at a low stress amplitude (or number of cycles higher than  $3.10^5$  cycles) (Fig. 16a). However, no particle could be observed at the crack initiation sites at high stress amplitudes (or low number of cycles) (Fig. 16b). It should be noted that, at high stress amplitude, some specimens show multiple crack initiation sites without intermetallic particles.

For the M5.5 state, SEM fractographic observations led to the conclusion that in the majority of cases, crack initiation occurs from an intermetallic particle (Fig. 17a), at high and low level stress amplitudes (or low and high number of cycles). Of the ten observed specimens, two do not have particles at the crack initiation site (an example is given in Fig. 17b). For these two specimens, the crack initiated at the area of the highest roughness (and highest peaks) on the surface. Both mechanisms occur at low and high number of cycles.

A first conclusion can be drawn from the fractographic results. The principal crack initiation mechanism for the polished and the milled surface states is initiation from intermetallic particles. As the overall surface roughness increases, fatigue life decreases. The role of intermetallic particle is to locate the crack initiation via the stress concentration that it generates.

In a previous study [16], the authors presented a specific method that makes it possible to precisely locate the position of the crack initiation site with respect to the surface topology of the milled specimens. This method led to the observation that crack initiation for these batches occurs randomly over the gauge length of the specimens, and rarely in the areas where the arithmetic roughness is maximum. However, for the batches with high surface roughness  $S_a$ , cracks are systematically located at the bottom of the milling grooves, but are randomly distributed along the bottom of the groove at areas of low and high linear roughness alike (see Fig. 18). From this, it can be concluded that linear roughness is not a suitable parameter to relate to the fatigue behavior [16].

**Fig. 9** Surface state after **a** pickling and **b** TSA anodizing

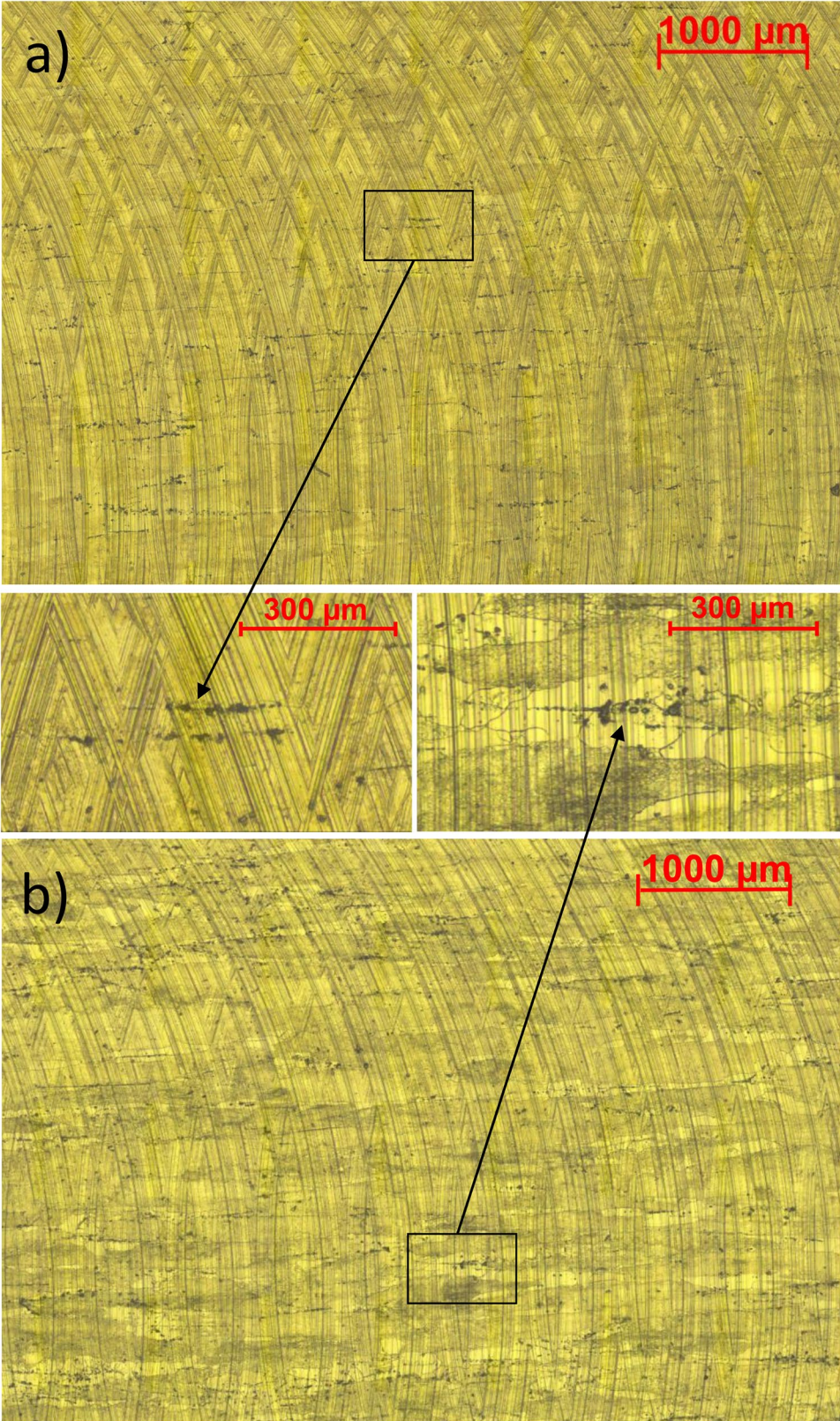
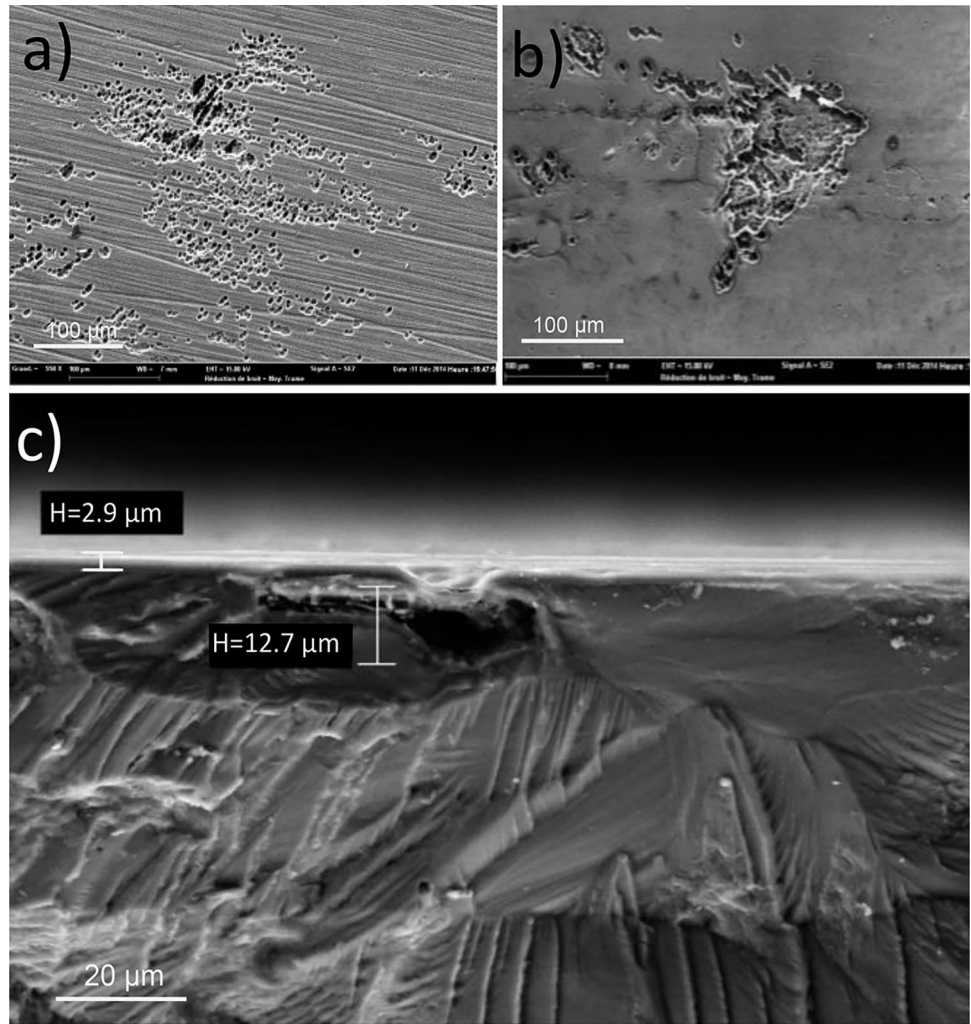


**Fig. 10** SEM observations of surface defect groups of **a** a pickled, **b** an anodized specimen and **c** (fractography of a specimen with a TSA anodizing layer of around  $3\ \mu\text{m}$ )



### 3.1.3 Effect of grinding on the fatigue behavior

For the grinded surface state G3.8, the fatigue strength is 157 MPa (see Fig. 19) and is very similar to the M1.1 milled

state in the high cycles domain. However, the S-N curve of these two configurations seems to differ in the low cycles domain for which the grinded state has a slightly reduced fatigue life. It seems that the grinding scratches are more

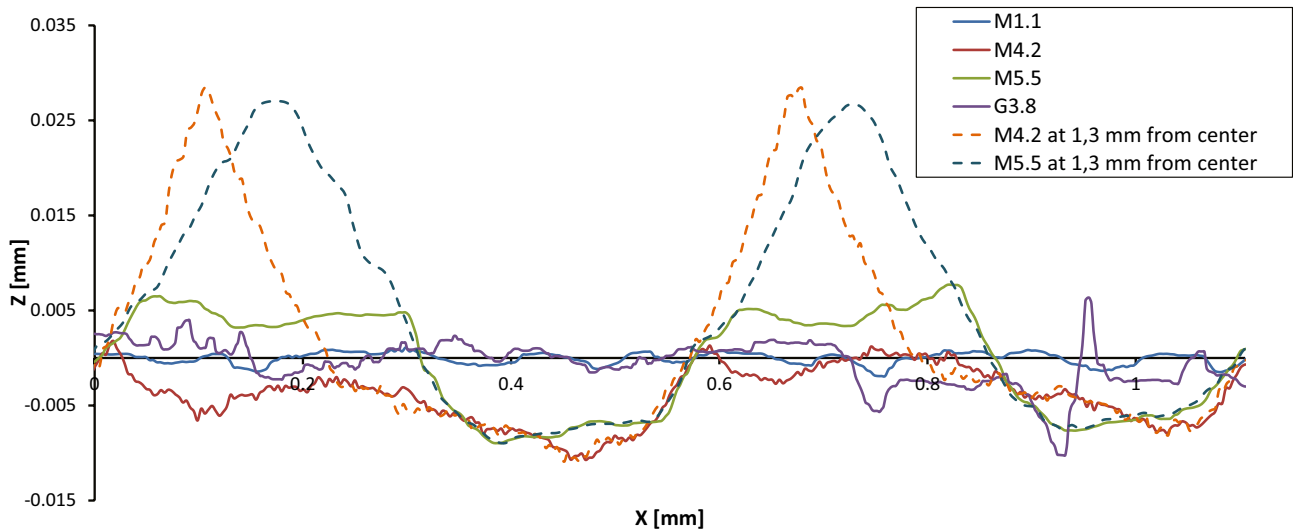


**Fig. 11** 2D roughness profiles for the milled and grinded batches

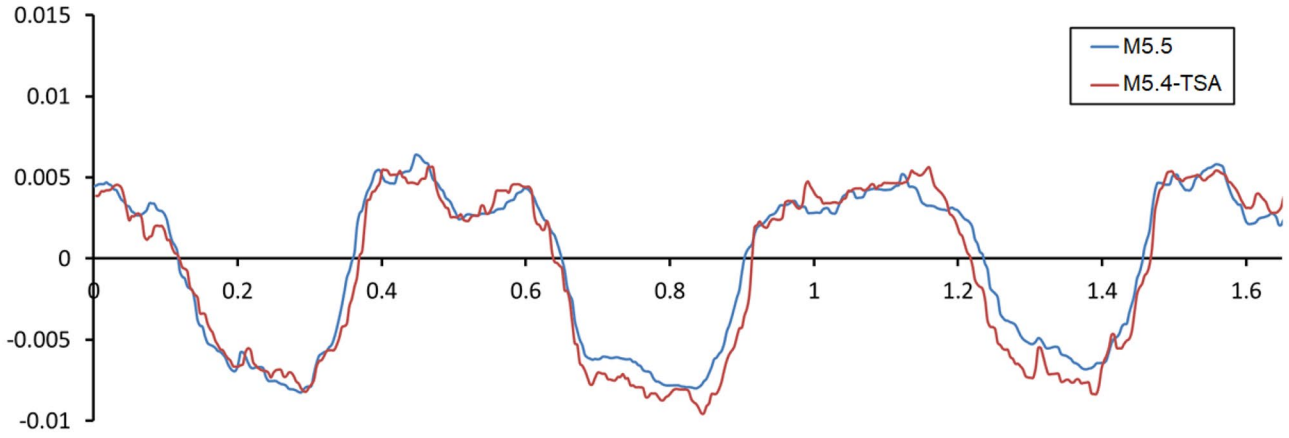


Fig. 12 The impact of TSA anodizing on surface roughness profile (M5.5 batch before and M5.4-TSA batch after surface treatment)

harmful in the low cycle fatigue domain (i.e., for higher stress amplitude).

For the grinded G3.8 batch, cracks initiate from the surface grinding scratches. These scratches can be up to  $10\ \mu\text{m}$  in depth and several millimeters in length (Fig. 20). In 6 out of 8 cases, no intermetallic particles are observed at the initiation site. At high stress amplitudes, multiple crack sites were identified. In some cases, crack initiation occurs at the corner of the specimen due to the scratch's harmfulness (2 out of 8 observed cases).

These observations as well as the fatigue strength results make it possible to draw several conclusions. Firstly, the scatter associated with the fatigue strength is significantly greater than previous surface states (see Table 5). This could be due to the surface topology, which is rather chaotic compared to the periodic roughness profiles seen on the previous batches. Secondly, the significant change in the surface topology causes a change in the damage mechanism whereby crack initiation occurs less frequently at intermetallic particles. Instead, cracks initiate due to the stress concentration generated at the grinding scratches. Despite the chaotic nature of the grinded surface, the global surface roughness  $Sa$  is similar for all the specimens and is lower than the  $Sa$  values for the M4.2 and M5.5 batches, which could explain

the higher fatigue strength (157 MPa). Also, it seems that the difference in the surface roughness between the M1.1 and the G3.8 batches does not have much of an impact on the fatigue resistance in the high cycle domain although the surface roughness goes from  $1.1\ \mu\text{m}$  to  $3.8\ \mu\text{m}$ . This could be due to the fact that scratches, although sharp and long, have depth smaller than the average grain size of the studied material in the depth direction (see Fig. 11).

### 3.1.4 Effect of TSA anodizing on the fatigue behavior

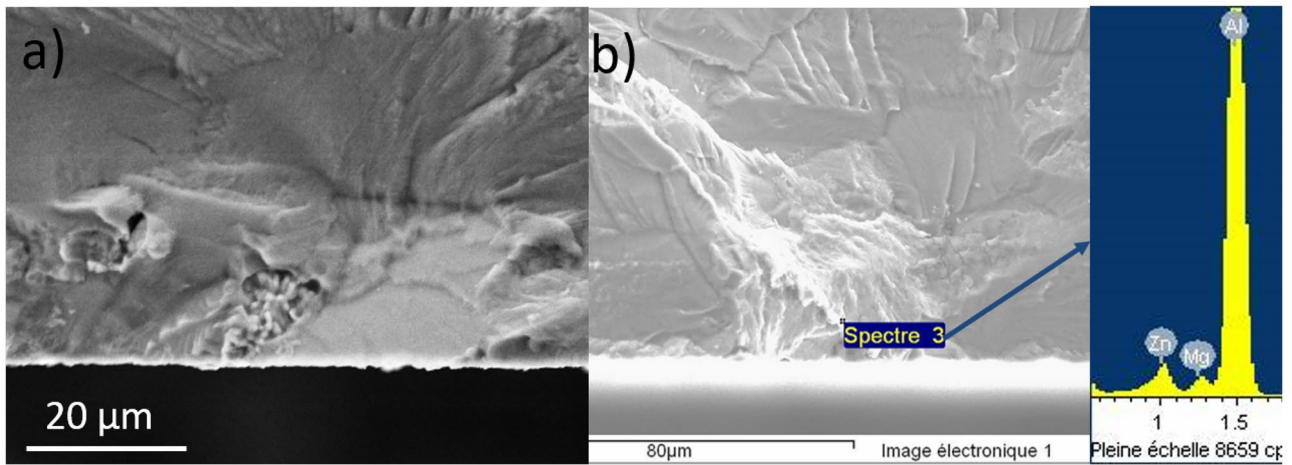
Surprisingly, the fatigue resistance is enhanced for the two anodized surface states. A gain of 15 MPa in the fatigue strength is observed for both the 0.9-TSA and 5.4-TSA batches, compared to the same batches without the surface treatment. Figure 21 presents the S-N curves for the two surface states before and after surface treatment. This surprising result is in agreement with the few results of the literature addressing this issue [13, 14], where the tartaric-sulfuric treatment was found to preserve fatigue strength.

Table 4 Surface roughness characteristics for the different batches

Surface State	$Sa\ (\mu\text{m})$	$Ra_{max}\ (\mu\text{m})$
P0	0.04	0.04
M1.1	1.1	1.02
M4.2	4.2	9.27
M5.5	5.5	7.1
G3.8	3.8	4.24
M0.9-TSA	0.9	1.04
M5.4-TSA	5.4	7.25

Table 5 Fatigue test results for the different surface states batches.  $\sigma_{-1}^-$  and  $\sigma_{-1}^+$  are the average fatigue strength and the standard deviation respectively

Surface State	$Sa\ (\mu\text{m})$	Fatigue strength		Tested Specimens
		$\sigma_{-1}^-$ (MPa)	$\sigma_{-1}^+$ (MPa)	
P0	0.04	174	5.3	15
M1.1	1.1	159	5.3	15
M4.2	4.2	141	5.3	15
M5.5	5.5	119	5.3	10
G3.8	3.8	157	9.5	10
M0.9-TSA	0.9	175	11	15
M5.4-TSA	5.4	134	5.3	10



**Fig. 13** Fractographic analysis of the P0 surface state: crack initiation at **a** an  $Al_7Cu_2Fe$  type particle, **b** no particles but presence of Mg, Al and Zn elements

After anodizing, the results of the M0.9-TSA batch are more scattered, with a standard deviation of approximately 11 MPa.

As for the damage mechanisms for the anodized surface states, SEM observations of the M0.9-TSA surface state show that the crack initiation sites are located at the pickling pits. As shown in Fig. 22, these pits are of different sizes and shapes and can achieve lengths of approximately  $88 \mu m$  (i.e., pit clusters in Fig. 22b) and depths around  $30 \mu m$ . For the M5.4-TSA batch, crack initiation always occurs

from a defect, either at pickling pits at the extreme surface for 50% of cases (see Fig. 23), or at intermetallic particle a few micrometers below the surface (see Fig. 24). Note that the pits are generated due the dissolution of the aluminum in the intermetallic particles during the pickling operation [11].

As seen in Fig. 25, the position of the crack initiation sites are randomly located at the bottom of the milling grooves. The stress concentration generated by these grooves, and moreover by the presence of a defect (pitting or particle) controls the crack initiation for the anodized batches.

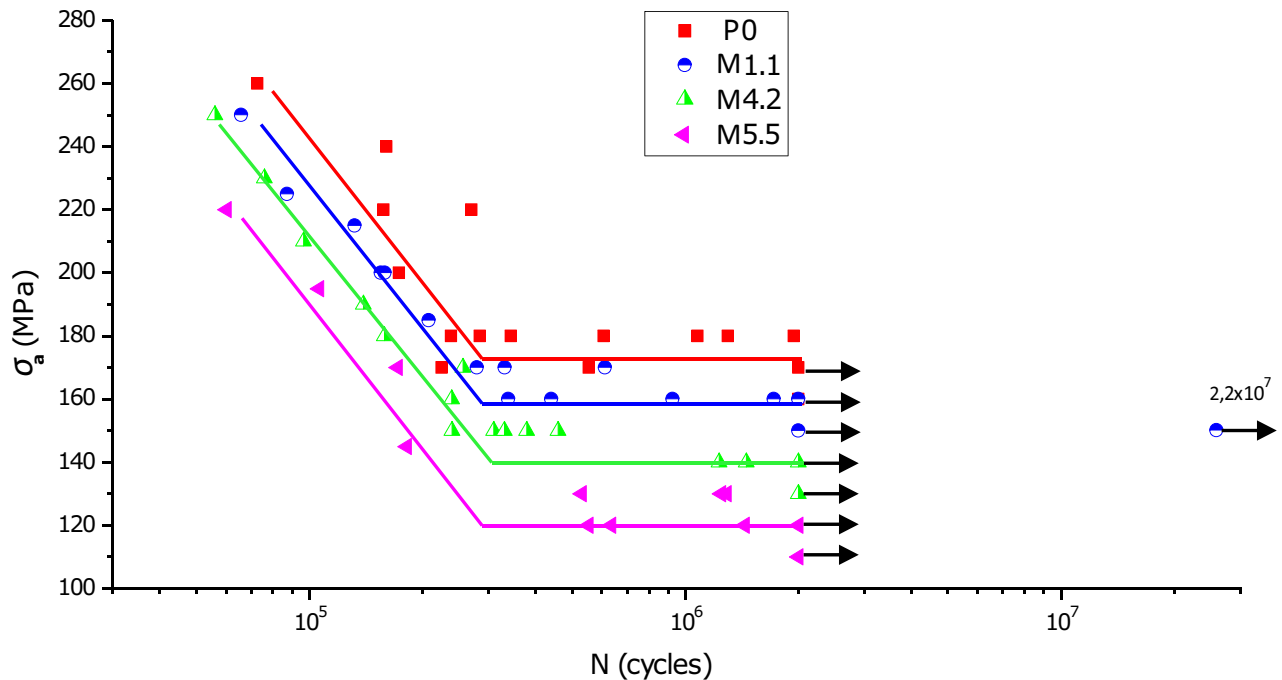


**Fig. 14** S-N curves of different surface states obtained by polishing and end milling

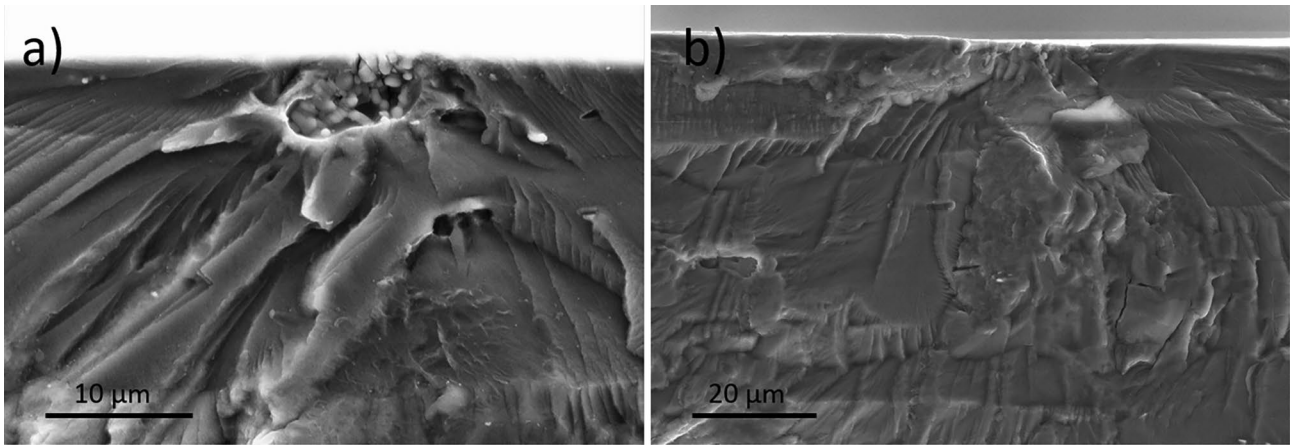


Fig. 15 M1.1 state: crack initiation from **a** a particle and **b** without an observable particle

Based on these observations and the fatigue test results, it can be concluded that the TSA process has very little effect on the surface topology and roughness of the substrate. Also, the fatigue damage mechanism remains unchanged before and after the surface treatment. Furthermore, despite the large pits observed on some specimen failure surfaces, the fatigue strength of the anodized batches is slightly better than those without surface treatment. This can be explained by the presence of the anodic layer that adheres perfectly to the substrate and probably improves the resistance to crack initiation. Note that no evidence of decohesion between the anodic layer and the substrate was detected on all of the analyzed fractographies for TSA anodized specimens. Note also that the TSA anodizing process does not seem to affect the pit population and morphology generated by the pickling process (see Fig. 9). For the rest of the analysis, we will make the assumption for all the batches that only the surface condition controls the fatigue strength. This assumption is slightly conservative for the TSA batches as it neglects the

positive impact of the anodic layer on the behavior for these batches.

It is clear, based on the results presented above, that the end milled and grinded surface topologies are quite complex and difficult to describe by a roughness parameter measured over a line ( $Ra$ ,  $Rt$ ,  $Rz$ ...). As shown on a previous paper [16], several other parameters ( $Sq$ ,  $Sz$ ) and/or their combination (Souto-lebel's parameter [23]) were tested against the observed fatigue behavior, however, the surface roughness  $Sa$  seems to be the best roughness parameter to characterize the effect of the surface topology on the fatigue behavior of the end milled parts. Figure 26 shows the evolution of the fatigue strength as a function of the  $Sa$  parameter on a bi-logarithmic graph. This graph is inspired by the Kitagawa-Takahashi diagram typically used to represent the evolution of the fatigue strength as a function of the defect size measure at the initiation site [24]. As can be seen in Fig. 26, for low  $Sa$  values (below around  $3 \mu m$ ) the fatigue strength seems to be defined by a plateau and not very sensitive to the

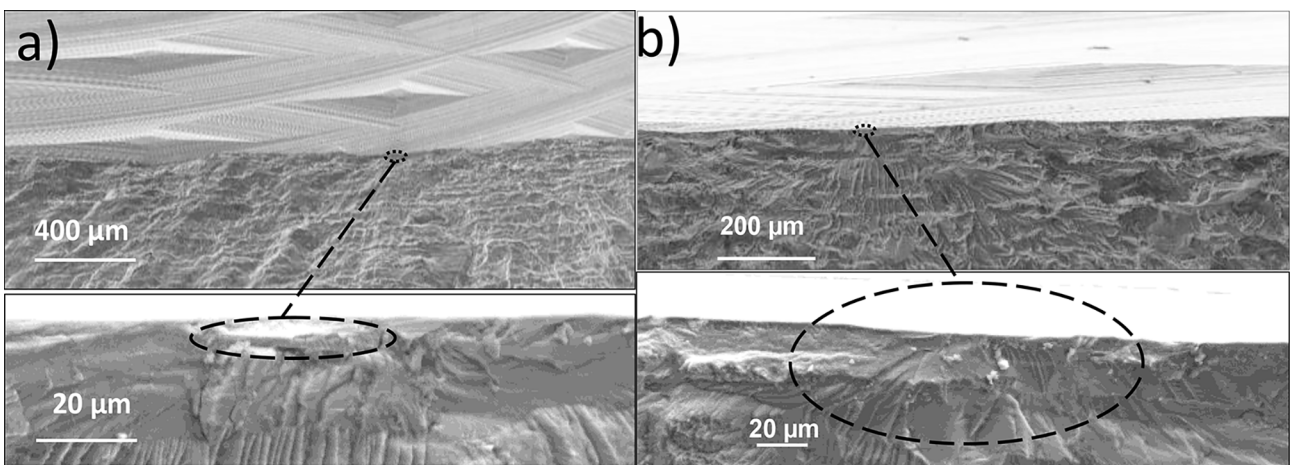


Fig. 16 M4.2 state: crack initiation from **a** a particle and **b** without an observable particle

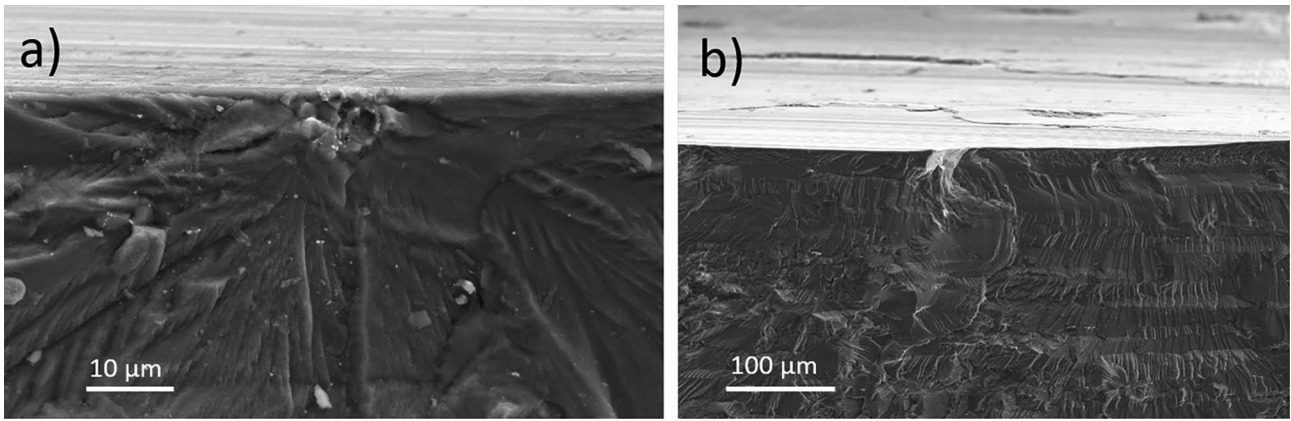


Fig. 17 M5.5 state: crack initiation from **a** a particle and **b** without an observable particle

$Sa$  value. Above the critical value of  $Sa$  of  $3 \mu m$ , the fatigue strength has higher sensitivity to the surface roughness. Note that for the 2 batches with anodized surface states M0.9-TSA and M5.4-TSA, the link between fatigue strength and the surface roughness  $Sa$  (Fig. 26) seems to follow the same trend as the batches without the surface treatment.

Figure 26 makes it possible to identify two distinct regions. The first region is a plateau corresponding to roughness values smaller than approximately  $Sa = 3,1 \mu m$ . In this domain, the fatigue strength is constant and is not affected by the surface roughness. The plateau is set, in this study, at the level of the reference batch P0, with a fatigue strength of 174 MPa. This threshold level seems to be a physical property below which no effect in terms of HCF occurs. Similar thresholds, presented in terms of Rz, were reported in [25, 26] for various steels. As mentioned previously, the grooves and scratches on the surface of the batches below

this threshold are smaller than the average material's grain size, which could explain their associated fatigue strength. In the second region of the graph, the progressive decrease in the fatigue strength can be directly linked to the surface roughness  $Sa$  via a power relation. The slope of the straight line in log-log space defining this relation is  $-0.5$  ( $\sigma_D = 313.Sa^{-1/2}$ ).

#### 4 Modelling of the surface states obtained via end milling process to link surface roughness to fatigue strength

In this section, the authors attempt to generate numerically a surface state that reproduces the experimental state obtained for the M4.2 and the M5.5 batches, using the milling parameters presented in Table 1. The aim of the simulation is to

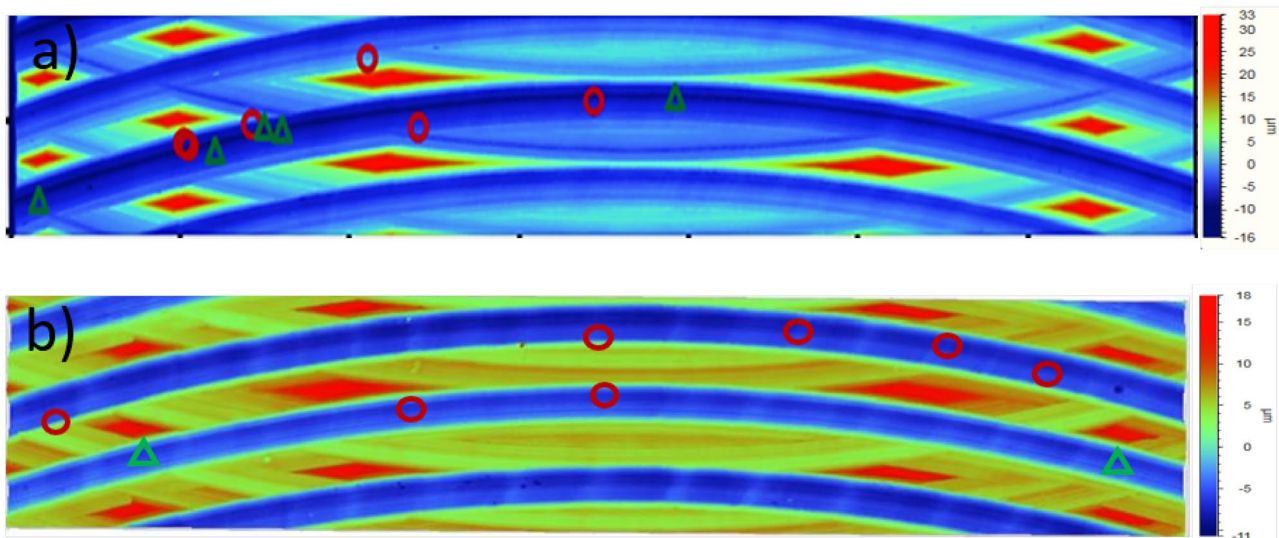
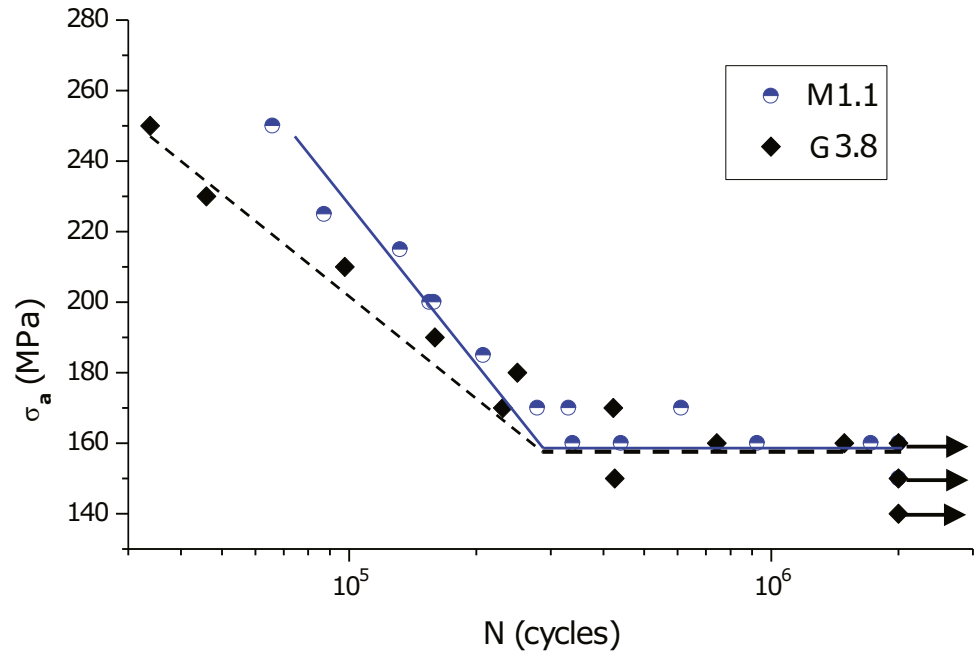


Fig. 18 Crack initiation positions for specimens of **a** M4.2 and **b** M5.5 states. The red circles represent crack initiations from an intermetallic particle, whereas the green triangles represent crack initiations without an observable particle

**Fig. 19** S-N curves of the end milled M1.1 and the grinded G3.8 configurations



link the milling conditions to the surface roughness and hence to the fatigue strengths shown in Fig. 26. For the simulations, only the macro geometrical aspects are considered. Other aspects such as residual stresses or microstructural effects are not considered, as their effect on the fatigue

strength are deemed to be secondary in our case, based both on the literature [2–4] and on the results of this study. Let’s recall that residual stresses as well as hardening can have an effect on the fatigue strength in different conditions (case of rolling milling [2]).

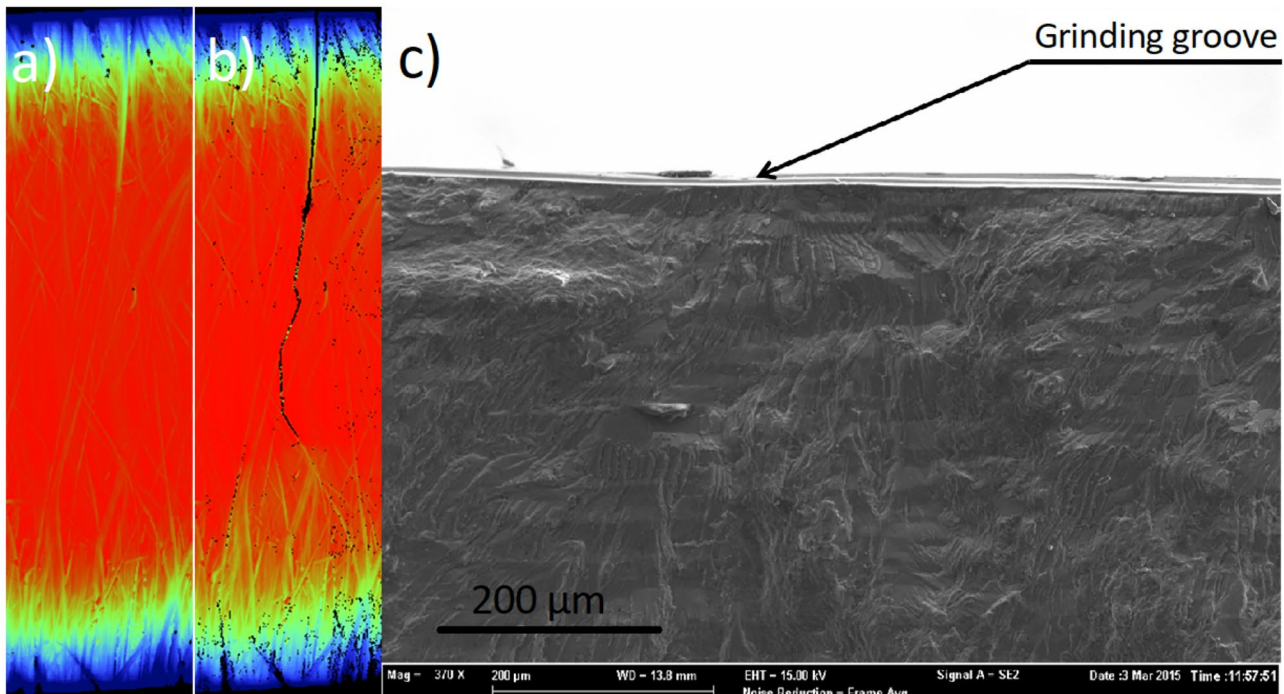


**Fig. 20** Crack initiation from grinding scratch: surface scan of the grinded face **a** before and **b** after cracking and **c** a SEM fractographic observation of the initiation site

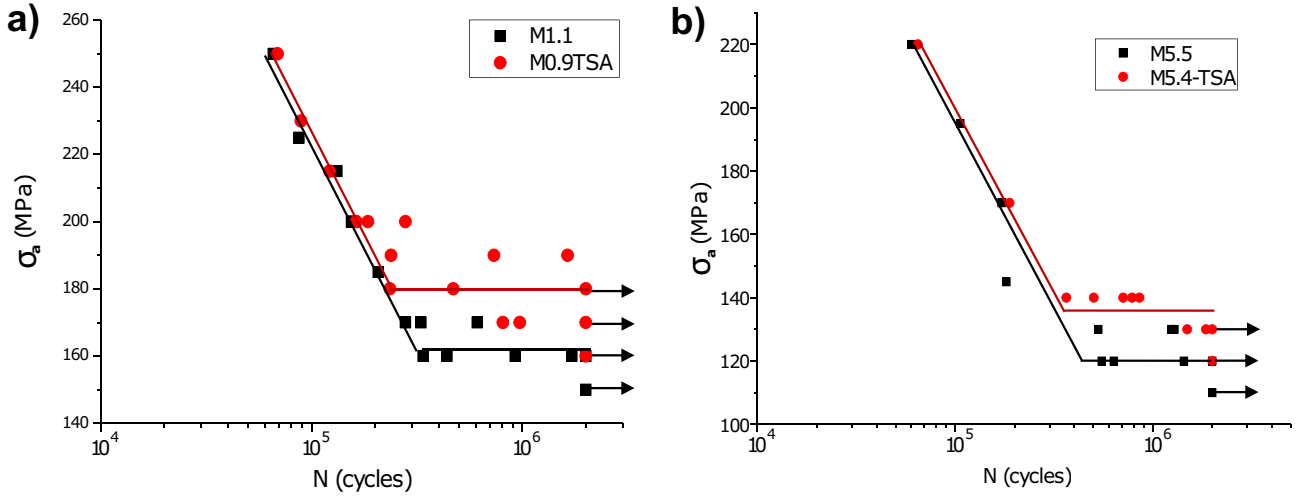


Fig. 21 S-N curves showing the influence of TSA on the fatigue strength: **a** M0.9-TSA batch and **b** M5.4-TSA batch

Based on the work of Godreau et al. [27], in order to realize the simulation of milled surfaces, the following three steps are required:

- Design of the tool.
- The movement of the tool while machining respecting the milling condition (rotational speed, feed rate, angle between the spindle axis and the milled surface).
- Extraction of the milled surface.

The simulations were conducted using the geometry and the milling conditions of the milling tool presented in Table 1. The simulated surface is 7mm x 1.1mm which corresponds to the width of the upper surface of the specimen and twice the Feed rate, respectively. As for the displacement of the tool, for each point M of the surface of the tool, for which the coordinates are  $(P_x; P_y; P_z)$ , the trajectory is defined by:

$$\begin{pmatrix} P'_x(\theta) \\ P'_y(\theta) \\ P'_z(\theta) \end{pmatrix} = \begin{pmatrix} P_x \\ P_y \\ P_z \end{pmatrix} * \begin{pmatrix} \cos(\theta)\cos(\alpha) & -\sin(\theta)\cos(\theta)\sin(\alpha) \\ \sin(\theta)\cos(\alpha) & \cos(\theta)\sin(\theta)\sin(\alpha) \\ -\sin(\alpha) & 0 & \cos(\alpha) \end{pmatrix} + \begin{pmatrix} ZF_z\theta \\ 2\pi \\ 0 \end{pmatrix} \quad (3)$$

where  $\theta$  = the spindle rotation angle,  $\alpha$  = the orientation angle between the tool and the workpiece and  $P'(\theta)$  = the new coordinates of point M on the surface of the tool.

Post-processing is then applied to extract a trajectory generated by the tool's displacement. A second and final post-processing makes it possible to discretize the simulated (x,y) plan to the desired resolution (in this case a resolution of 10  $\mu\text{m}$  is used). The trajectory is then superimposed on the grid. Within each square of this grid, the minimum value in the z direction of the trajectory is selected. This value will lead to the realization of the simulated milled surface. A point cloud is finally extracted and visualized via Vision64 software.

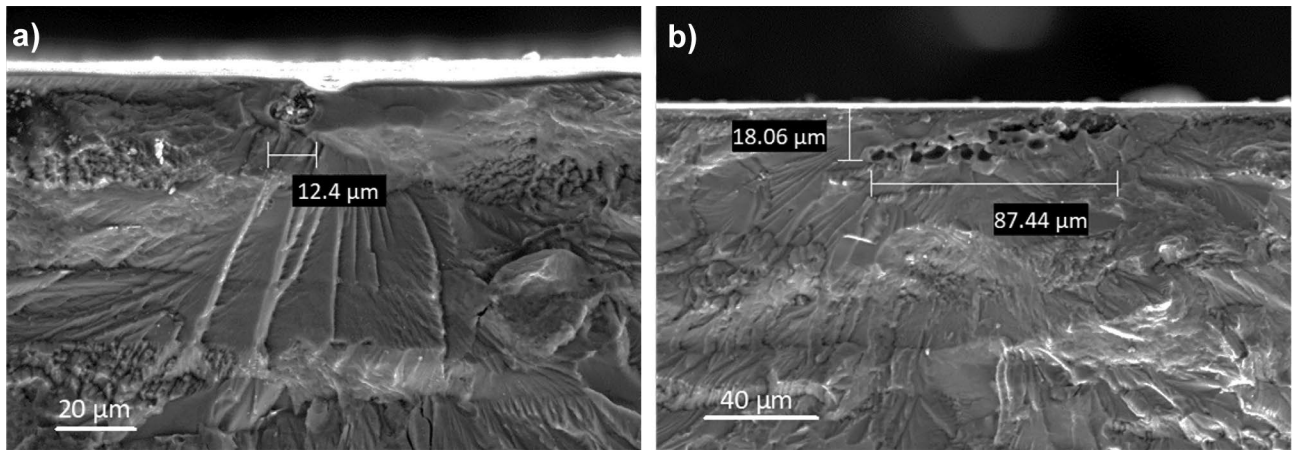


Fig. 22 M0.9-TSA: crack initiation from pickling pits

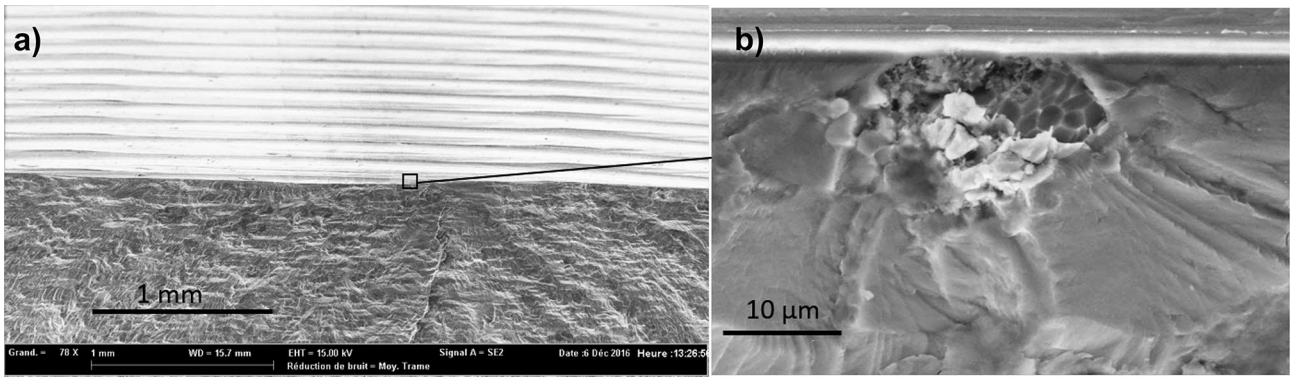


Fig. 23 M5.4-TSA : crack initiation from a pickling pit

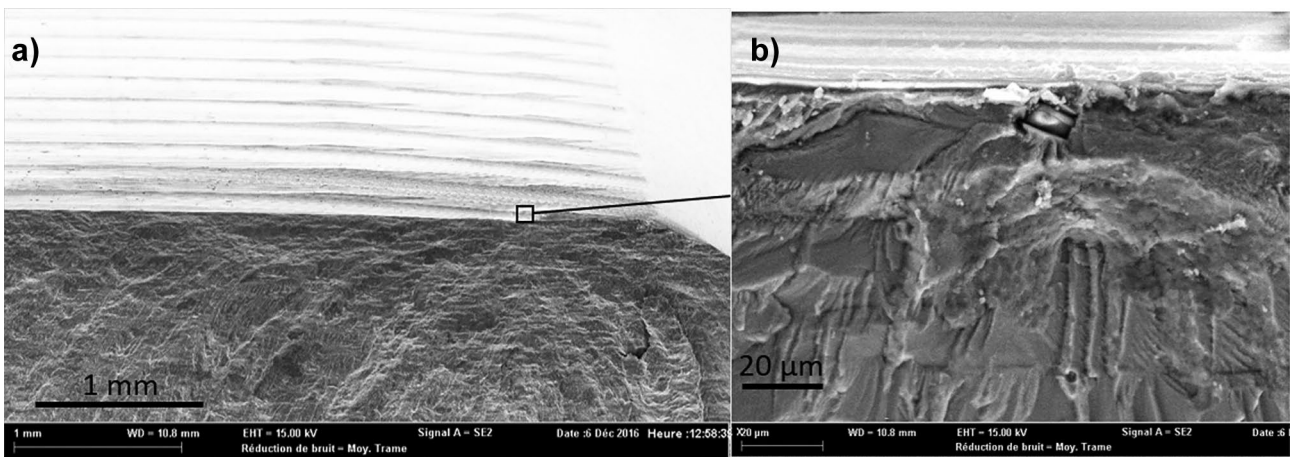
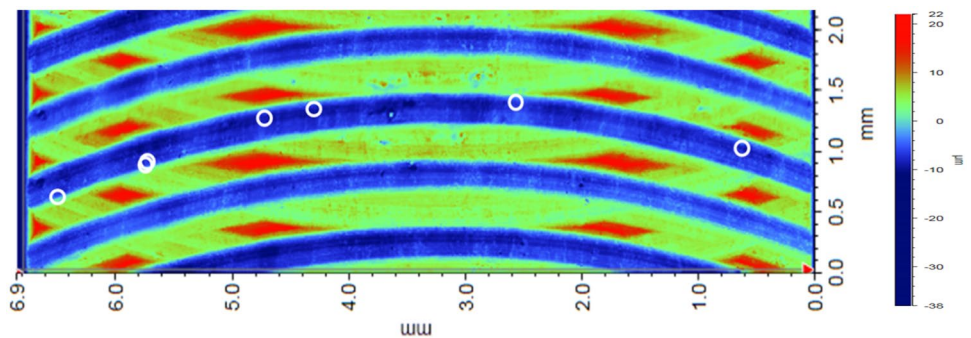


Fig. 24 M5.4-TSA : crack initiation from an intermetallic particle

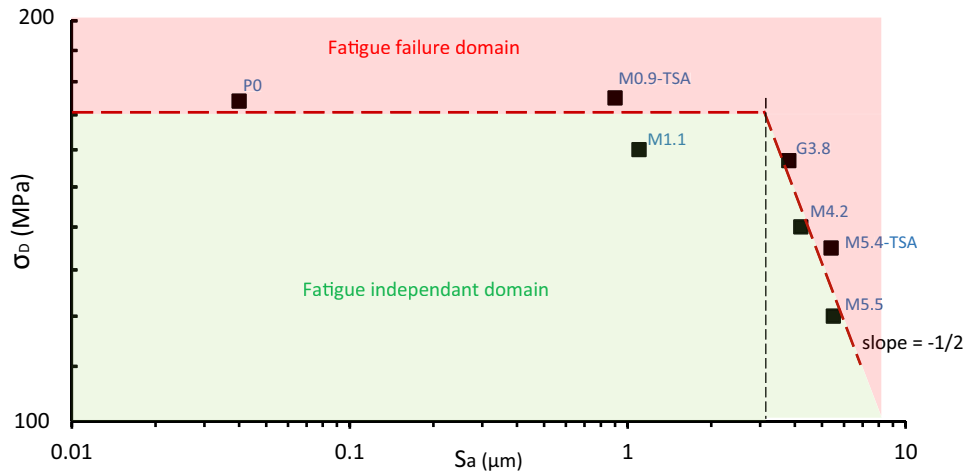
Fig. 25 M5.4-TSA: positions of the crack initiation sites at the bottom of milling grooves



Two configurations are tested, the first represents a slightly tilted tool and is used to reproduce the M4.2 surface state (tilt angle of  $0.014^\circ$ ) (see Table 1). The second configuration has a tilt of  $0.05^\circ$  in order to reproduce the M5.5 surface state. When considering a tool diameter of  $\varnothing 20$  mm, a slight tilt is capable of greatly modifying the surface state. Figure 27 shows 3D comparison between the real and

simulated surface states, while Fig. 28 presents 2D roughness profiles taken at different positions of the generated surface states for these two tilt configurations. The altitude at the bottom of the milling marks varies from one groove to another due to the tool/part tilt. The altitude difference between the peaks and the bottoms of the grooves is up to  $47 \mu\text{m}$  for the simulated roughness profiles. It can be seen

**Fig. 26** Kitagawa-Takahashi type diagram, expressed in terms of the parameter  $S_a$  that highlights the existence two damage mechanism regions



that the generated surfaces successfully describe the global surface geometries. However, differences due to irregularities at a lower scale can be observed between the experimental and numerical roughness profiles. Figure 28 shows that the numerical profiles have greater depth and height when compared to the real profiles at different positions (i.e., at 0.7 mm along the x axis for the M4.2 batch). This difference results in much higher predicted surface roughness values

than the experimentally measured values for the M4.2 and the M5.5 surface states. The estimated  $S_a$  value is  $6 \mu\text{m}$  for the M4.2 state and  $8.3 \mu\text{m}$  for the M5.5 state. This is approximately 30% and 33% higher than the experimental values, respectively.

According to similar studies such as [28–31], this difference is provoked mainly by the physical imperfections of the machining system. Factors such as cutting tool vibration,

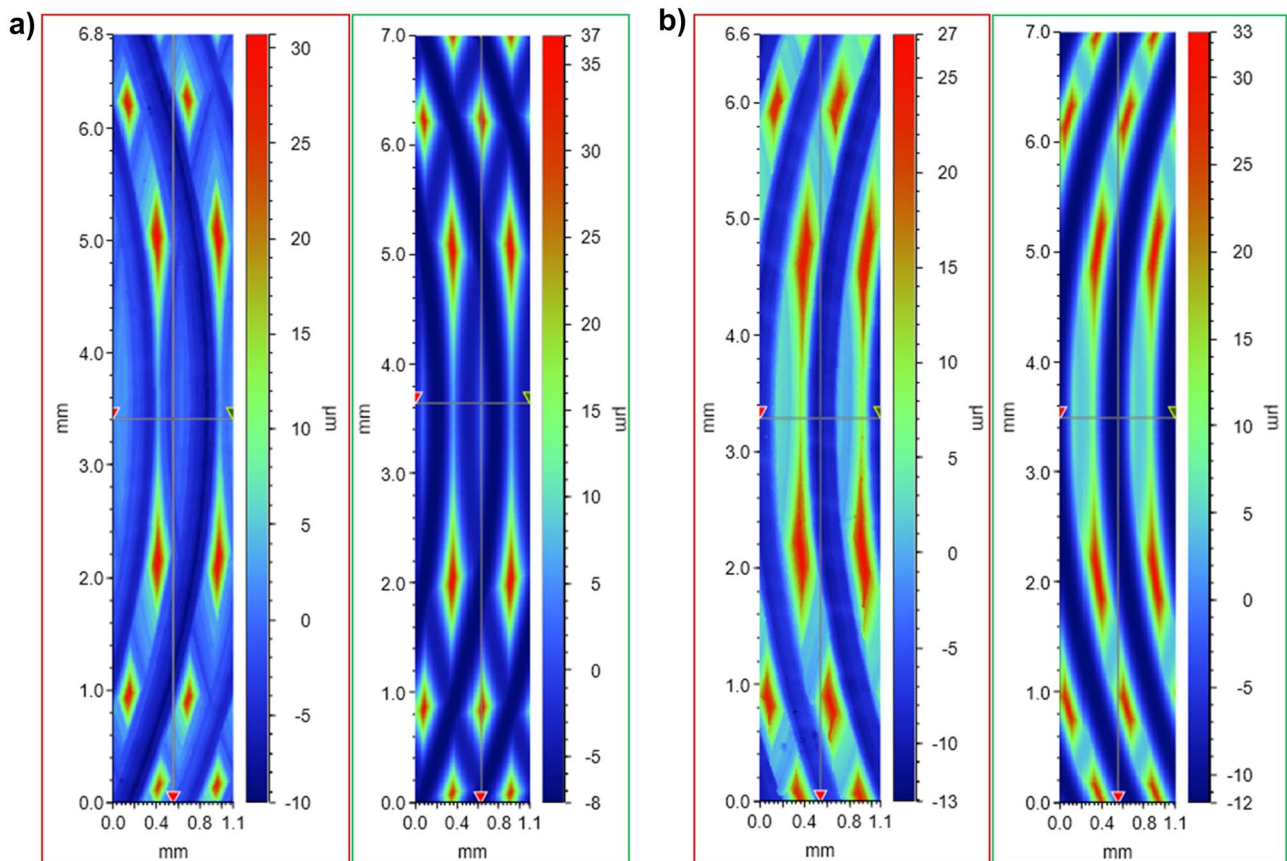


**Fig. 27** Comparison between 3D profiles of **a** the M4.2 and **b** the M5.5 surface states (red frame) and the simulated surface states (green frame)

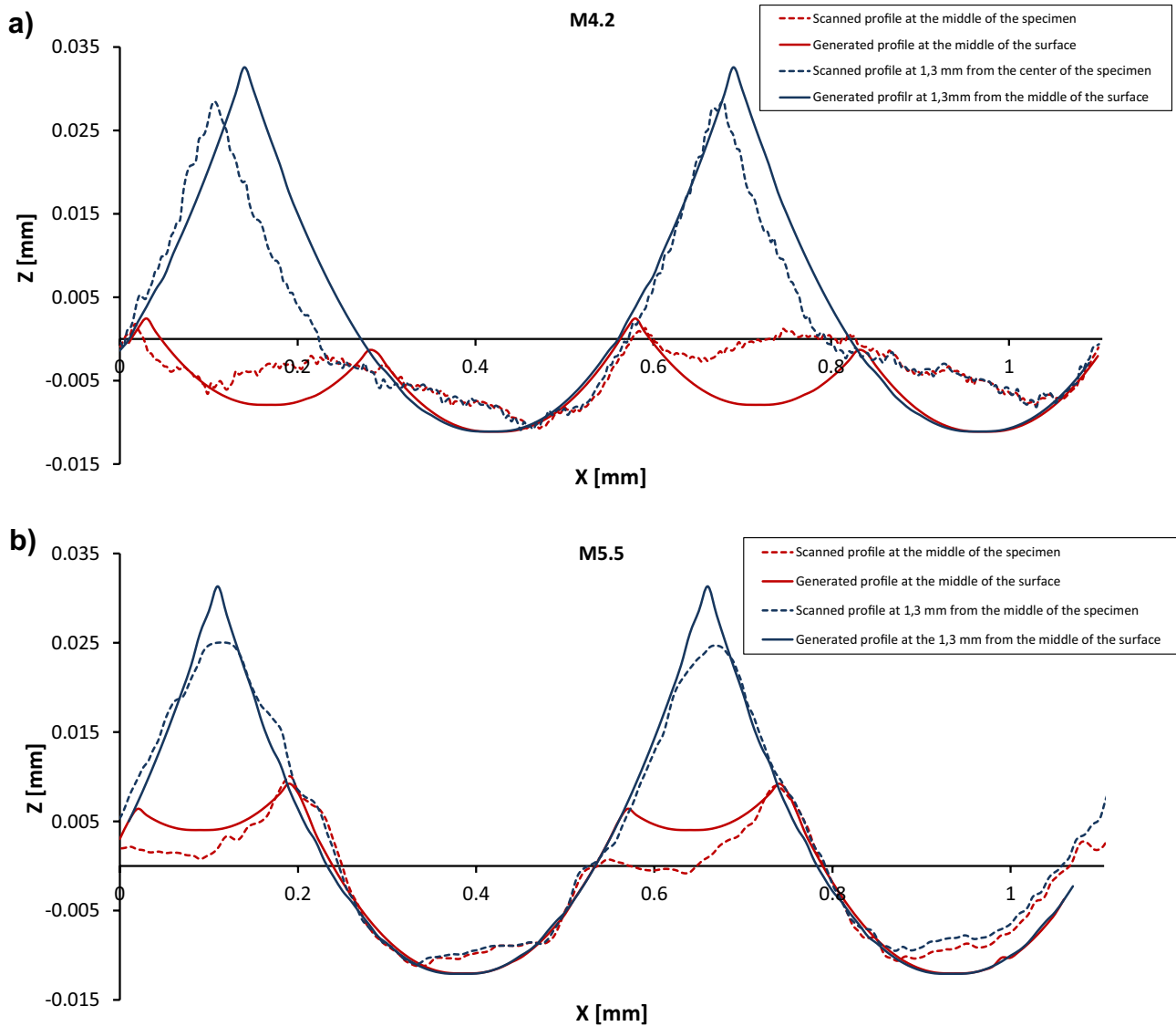


Fig. 28 Comparison between 2D roughness profiles of **a** the M4.2 and **b** the M5.5 surface states and the simulated roughness profiles

defects in the homogeneity of the work piece material, undeformed chip thickness variation, built-up edge and tearing of the work piece material play roles at different levels in altering the generated profile and hence the global surface roughness. Random wrinkles can also be generated depending on the tool's tilt and the rate of material's extraction at the front and the back of the cutting tool [32].

When correlating the surface roughness obtained via simulations with the fatigue strength results shown in Fig. 26, the error in the predicted  $S_a$  values results in conservative predictions for the fatigue strength of around 18% for the M4.2 batch (115 MPa instead of 141 MPa) and 16% for the M5.5 batch (100 MPa instead of 119 MPa). Since the offset is similar for both batches, it could be taken into account in the simulation, once verified on a test batch, for better

fatigue strength prediction. The knowledge of the milling cutting conditions makes it possible, via the proposed method, to predict the surface roughness and therefore, based on the modified Kitagawa diagram, to predict the fatigue strength for the AA7050. This tool can be very useful for predicting fatigue life from a wide variety of tool paths.

## 5 Conclusions

This paper presents a comprehensive experimental study into the effect of surface state on the fatigue strength of the AA7050 alloy. The different surfaces studied are: polished, end milled with 3 different levels of roughness, grinded, and two end milled configurations followed by a tartaric-sulfuric anodizing treatment.

The results of the fatigue tests as well as the associated damage mechanisms observed for each surface state have been presented. The main conclusions are as follows:

- The fatigue behavior of the AA7050 alloy is linked to the global surface roughness, described by the  $S_a$  parameter. The arithmetic roughness  $R_a$  is not suitable to describe the fatigue behavior of end milled and grinded surfaces.
- For the milled surface states, an increase in surface roughness results in a decrease in the fatigue strength. However, it is necessary to highly degrade the surface roughness in order to observe a decrease in the fatigue strength of the AA7050 alloy.
- The grinding process generates a chaotic surface state, increases scatter in the fatigue strength and modifies the damage mechanism. After grinding, the average high cycle fatigue strength is similar to the standard milled state M1.1.
- The tartaric-sulfuric anodizing treatment (TSA) has a very small influence on the topology of the substrate and the surface roughness. The damage mechanism remains the same as the milled batches. Surprisingly however, the anodized batches have slightly better fatigue resistance, regardless of the initial surface state. This result is in agreement with the small number of publications in the literature that address this issue [13, 14].
- The modified Kitagawa diagram, combined with the numerical simulations of the surface topography, makes it possible to establish a link between the cutting conditions, the surface roughness and hence the fatigue strength.

**Author Contributions** All authors contributed to the study conception and design. Material preparation and data collection were performed by F. Abroug and E. Pessard. Analysis, discussions and validation were performed by F. Abroug, E. Pessard G. Germain and F. Morel. The first draft of the manuscript was written by F. Abroug and all authors commented on previous versions of the manuscript. All authors read and approved the final manuscript.

**Availability of data and material** All data generated or analyzed during this study are included in the present article.

## References

1. Novovic D, Dewes RC, Aspinwall DK, Voice W, Bowen P (2004) The effect of machined topography and integrity on fatigue life. *Int J Mach Tools Manuf* 44(2–3):125–134
2. Brunet, S. (1991). Influence des contraintes résiduelles induites par usinage sur la tenue en fatigue des matériaux métalliques aéronautiques (Doctoral dissertation, Paris, ENSAM)
3. Guillemot, N. (2010). Prise en compte de l'intégrité de surface pour la prévision de la tenue en fatigue de pièces usinées en fraisage (Doctoral dissertation, École normale supérieure de Cachan-ENS Cachan)
4. Chaussumier M, Mabru C, Chieragatti R, Shahzad M (2013) Fatigue life model for 7050 chromic anodized aluminium alloy. *Procedia Engineering* 66:300–312
5. Quan F, Chen Z, Ye H, Cui C, Cui Y (2021) Study of the effect of surface roughness on fatigue strength of GH4169 based on indirect evaluation of the notch root radius. *Int J Fatigue* 152:106440
6. Jouini N, Revel P, Thoquenne G (2020) Influence of surface integrity on fatigue life of bearing rings finished by precision hard turning and grinding. *J Manuf Process* 57:444–451
7. Xu Z, Dunleavy J, Antar M, Hood R, Soo SL, Kucukturk G, Hyde CJ, Clare AT (2018) The influence of shot peening on the fatigue response of Ti-6Al-4V surfaces subject to different machining processes. *Int J Fatigue* 111:196–207
8. Xun L, Guan CM, Zhao P (2017) Influences of milling and grinding on machined surface roughness and fatigue behavior of GH4169 superalloy workpieces. *Chin J Aeronaut* 31(6):1399–1405
9. Liu D, Shi Y, Lin X, Xian C, Gu Z (2019) Study on avoiding the knife marks of the blade after polishing by flap disc. *Int J Adv Manuf Technol* 105(5):2733–2744
10. Ås SK, Skallerud B, Tveiten BW (2008) Surface roughness characterization for fatigue life predictions using finite element analysis. *Int J Fatigue* 30(12):2200–2209
11. Shahzad M, Chaussumier M, Chieragatti R, Mabru C, Aria FR (2010) Influence of surface treatments on fatigue life of Al 7010 alloy. *J Mater Process Technol* 210(13):1821–1826
12. Savas TP, Earthman JC (2008) Surface characterization of 7075–T73 aluminum exposed to anodizing pretreatment solutions. *J Mater Eng Perform* 17(5):674–681
13. Lee E, Jeong Y, Kim S (2012) SN Fatigue behavior of anodized 7050–T7451 produced in different electrolytes. *Metall Mater Trans A* 43(6):2002–2011
14. Mauduit, A. (2013). Comparaison OAS - OAST en termes de faïençage, corrosion, fatigue. Les rendez-vous technologiques «Les traitements de surface des alliages légers» Cetim-Certec
15. Paz Martínez-Viademonte M, Abrahimi ST, Hack T, Burchardt M, Terryn H (2020) A review on anodizing of aerospace aluminum alloys for corrosion protection. *Coatings* 10(11):1106
16. Abroug F, Pessard E, Germain G, Morel F (2018) A probabilistic approach to study the effect of machined surface states on HCF behavior of a AA7050 alloy. *Int J Fatigue* 116:473–489
17. Gupta VK, Agnew SR (2011) Fatigue crack surface crystallography near crack initiating particle clusters in precipitation hardened legacy and modern Al-Zn-Mg-Cu alloys. *Int J Fatigue* 33(9):1159–1174
18. Nizery, E. (2015). Amorçage et propagation des fissures de fatigue dans les alliages d'aluminium 2050-T8 et 7050-T7451 (Doctoral dissertation, Lyon, INSA)

19. Dixon WJ, Mood AM (1948) A method for obtaining and analyzing sensitivity data. *J Am Stat Assoc* 43(241):109–126
20. ISO-12107, 2012, Metallic materials - fatigue testing - statistical planning and analysis of data, Geneva
21. Li JF, Zheng ZQ, Li SC, Chen WJ, Ren WD, Zhao XS (2007) Simulation study on function mechanism of some precipitates in localized corrosion of Al alloys. *Corros Sci* 49(6):2436–2449
22. Shahzad, M. (2011). Influence de la rugosité et des traitements d'anodisation sur la tenue en fatigue des alliages d'aluminium aéronautiques 2214 et 7050 (Doctoral dissertation)
23. Souto-Lebel, A. (2014). Rôle de l'intégrité de surface dans la tenue en fatigue d'un acier bainitique après fraisage de finition (Doctoral dissertation, Cachan: ENS Cachan)
24. Kitagawa H (1976) Applicability of fracture mechanics to very small cracks or the cracks in the early stage. *Proc. of 2nd ICM. Cleveland* 1976:627–631
25. Liu G, Huang C, Zhao B, Wang W, Sun S (2021) Effect of machined surface integrity on fatigue performance of metal workpiece: A review. *Chinese Journal of Mechanical Engineering* 34(1):1–16
26. Siebel E (1957) Influence of surface roughness on the fatigue strength of steels and non-ferrous alloys. *Eng Dig* 18:109–112
27. Godreau, V. (2017). Extraction des connaissances à partir des données de la surveillance de l'usinage (Doctoral dissertation, Nantes)
28. Franco P, Estrems M, Faura F (2008) A study of back cutting surface finish from tool errors and machine tool deviations during face milling. *Int J Mach Tools Manuf* 48(1):112–123
29. Lavernhe S, Quinsat Y, Lartigue C, Brown C (2014) Realistic simulation of surface defects in five-axis milling using the measured geometry of the tool. *Int J Adv Manuf Technol* 74(1):393–401
30. Wang P, Zhang S, Yan ZG (2017) Study on surface defects in five-axis ball-end milling of tool steel. *Int J Adv Manuf Technol* 89(1):599–609
31. Lazkano X, Aristimuño PX, Aizpuru O, Arrazola PJ (2022) Roughness maps to determine the optimum process window parameters in face milling. *Int J Mech Sci* 221:107191
32. Dong Y, Li S, Zhang Q, Li P, Jia Z, Li Y (2021) Modeling and analysis of micro surface topography from ball-end milling in a trochoidal milling mode. *Micromachines* 12:1203